

Automatic Selection of Parameters for Vessel/Neurite Segmentation Algorithms

Muhammad-Amri Abdul-Karim, Badrinath Roysam, *Member, IEEE*, Natalie Dowell-Mesfin, Andreas Jeromin, Murat Yuksel, *Member, IEEE*, and Shivkumar Kalyanaraman, *Member, IEEE*

Abstract— An automated method is presented for selecting optimal parameter settings for vessel/neurite segmentation algorithms using the minimum description length principle and a recursive random search algorithm. It trades off a probabilistic measure of image-content coverage, against its conciseness. It enables non-expert users to select parameter settings objectively, without knowledge of underlying algorithms, broadening the applicability of the segmentation algorithm, and delivering higher morphometric accuracy. It enables adaptation of parameters across batches of images. It simplifies the user interface to just one optional parameter, and reduces the cost of technical support. Finally, the method is modular, extensible, and amenable to parallel computation.

The method is applied to 223 images of human retinas and cultured neurons, from four different sources, using a single segmentation algorithm with 8 parameters. Improvements in segmentation quality compared to default settings using 1000 iterations ranged from 4.7 – 21%. Paired *t*-tests showed that improvements are statistically significant ($p < 0.0005$). Most of the improvement occurred in the first 44 iterations. Improvements in description lengths and agreement with the ground truth were strongly correlated ($\rho = 0.78$).

EDICS—2-SEGM Segmentation; 2-MODL Modeling; 2-ANAL Analysis

Manuscript received November 23, 2004; revised May 5, 2005. This work was supported in part by the Center for Subsurface Sensing and Imaging Systems (NSF ERC, Award EEC-9986821), MicroBrightField Inc., MARA of Malaysia, NIH, NIBIB, R01-0000359, the Nanobiotechnology Center (NSF STC ECS-9876771), NSF NeTS-NR 0435259, and Rensselaer Polytechnic Institute.

M.-A. Abdul-Karim, M. Yuksel and S. Kalyanaraman are with the Rensselaer Polytechnic Institute, Troy, NY 12180 USA (email: {abdulm,yuksem,shivkuma}@ecse.rpi.edu).

B. Roysam is with the Rensselaer Polytechnic Institute, Troy, NY 12180 USA (phone: 518-276-8067; fax: 518-276-8715; e-mail: roysam@ecse.rpi.edu).

N. Dowell-Mesfin is with The Wadsworth Center, NYS Department of Health, Albany, NY 12237 USA (email: dowell@wadsworth.org).

A. Jeromin is with the Baylor College of Medicine, Houston, TX 77030 USA (email: jeromin@www.clm.utexas.edu).

I. INTRODUCTION

One practical barrier to more widespread adoption of automated image analysis systems in quantitative biomedicine is the need to adapt/customize them to cope with biological variability. To achieve this, algorithm designers are forced to incorporate user-settable parameters. Users are faced with the difficulty of selecting these parameters without sufficient knowledge of the internal mechanisms. Time-consuming manual trial-and-error, as well as extensive developer support is often necessary to properly configure the software for a given application. Even then, these settings are subjective, and there is no assurance of optimality. Currently, settings for these algorithms are chosen empirically (e.g., [1-4]) or formulated heuristically (e.g.,[5]).

Accuracy of extracted measurements may also be affected by different algorithm settings. For example, Fig. 1a shows a phase contrast image of cultured neurites grown on an imprinted surface with known orientations of 45° and 90° . Panel (b) displays the automatically-generated traces using default settings. Panel (c) displays the traces obtained with automatically selected parameters using the method presented in this paper. The normalized angular histogram of measured segment orientations extracted from the automatically-generated traces is displayed in panel (d). Note the correct peak at 45° obtained using automatically-selected settings vs. 34° using default settings.

Of particular interest (but not limited) to this work is automated segmentation of tube-like structures (e.g., blood vessels and neurites) in biomedical images [1-28]. The primary goal is to enable a non-expert user to select parameters effectively, and objectively, treating the segmentation software as a “black box.” The secondary goal is to enable the algorithm developer to modify the internal details while maintaining a consistent and simple external interface; and to minimize the cost of technical support.

The rationale behind the proposed parameter selection method is that automated image analysis systems are expected to perform a non-trivial data reduction, extracting as much of the structural content in the image as possible, and expressing it concisely - in terms of instances and descriptive parameters of object models. In the fitting of these models to the image data, a tradeoff must be made between the

fitting error, and conciseness of the representation. This requires a quantitative metric to evaluate the segmentation quality along these two terms.

The proposed metric, based on the minimum description length (MDL) principle [29, 30], can be thought of as an adaptation to vessel/neurite segmentation from the generic formulation for image-partitioning as proposed by Leclerc [31]. The idea is to choose the optimal segmentation, and the corresponding optimal parameter settings, from a set of computable segmentations that correspond to different parameter settings. Currently, segmentation quality metrics have been devised for low-level vision tasks such as edge-detection [32-38] and image-partitioning [31, 39-42], but not for higher-level tasks such as vessel/neurite segmentation. Unlike the method published by Chalana and Kim [41, 43], the proposed metric for vessel/neurite segmentation does not require manual (or estimated [44]) ground truth segmentation. Also, unlike related works by Min *et al.* [45] for range image segmentation and the closed-loop reinforcement learning framework by Peng and Bhanu [46], the proposed parameter selection method is fully unsupervised.

Once the metric is defined, the vessel/neurite segmentation algorithm can be enclosed in a closed-loop optimization framework as shown in Fig. 2b. For the image segmentation problems of interest, it is rational to seek approximate solutions within a defined time frame, rather than truly global optima. In this work, a recursive random search based algorithm [47] is chosen to efficiently search for the optimal parameter settings. The proposed approach is modular by design. This is imperative due to the already high and growing complexity of modern segmentation software, making it impractical to interface with internal routines. A similar statement could be made concerning global optimization software. Modularity also enables substitutions of algorithms written by different groups.

II. SUMMARY OF RELATED LITERATURE

This work draws upon four main bodies of literature: (i) automated/quantitative/objective segmentation evaluation; (ii) MDL estimation; (iii) global optimization; and, (iv) automated vessel/neurite segmentation algorithms.

The traditional approach to evaluating segmentation algorithms is by visual inspection [33]. Significant progress has been made on automated approaches [48]. Metrics for segmentation evaluation [32-36, 39, 44, 49-52] can be either goal-oriented, i.e., evaluation based on the performance of post-segmentation steps such as pattern classification [50], based on other application-guided criteria such as the probability of false detection [35, 36, 49], or based on mismatch with manual ground truth segmentations (e.g., [52]). Most of them are specific for low-level vision tasks, such as edge detection [32-38] and region growing [31, 39], but are mentioned here nevertheless since they usually form the foundations of the more complex and specialized image segmentation algorithms (e.g., [3, 10]).

The MDL principle [30] offers a systematic way to obtain an objective balance between segmentation conciseness and coverage [29, 31, 42]. In this paper, we present a MDL-based variational formulation [31, 40, 42], similar to the Mumford-Shah approach for segmentation [39].

In the field of global optimization, genetic algorithms [53] and simulated annealing methods [54] are widely used since they require little *a priori* domain-specific information. However, these algorithms are mainly designed to seek full optimization and were found to lack initial efficiency for our application. Controlled random search [55], is also often considered for such cases. These are also known as stochastic optimization algorithms, mainly based on random sampling methods [47, 56], as opposed to deterministic algorithms (e.g., [57]). To improve efficiency, they are normally combined with local search techniques, such as steepest descent [58] and pattern search [59]. Limitations of global optimization algorithms are discussed in [60, 61].

Automated segmentation of tube-like structures in biological images, especially neurons [4, 6-9] and blood vessels [5, 10-24], are of particular interest to this work. These references are just a sparse sampling of the literature in this area, and the interested reader is referred to the literature review sections of these publications.

III. GENERAL OBJECTIVE FUNCTION

Although our immediate interest is the segmentation of tube-like objects, the description that

follows is presented more generally to enable the reader to adapt this approach to other applications and object types. A segmentation algorithm can be considered a function $f: \{\mathcal{I}, \xi\} \rightarrow \mathcal{M}$ that maps an image \mathcal{I} to a segmentation \mathcal{M} , using a parameter vector (“settings”) $\xi \in \Omega$ (see Fig. 2a). Our goal is to automate the search for the optimal $\hat{\xi}$ that yields the optimal $\hat{\mathcal{M}}$ in some practically useful sense.

The optimal segmentation $\hat{\mathcal{M}}$ must be chosen from the set of all computable segmentations $\{\mathcal{M}^i\}$, obtained by varying segmentation algorithm parameters ξ . The superscript i denotes the i^{th} iteration in the search of the optimal parameters $\hat{\xi}$. If a prior probability can somehow be assigned to each segmentation, maximum *a-posteriori* (MAP) can be used [31]. This requires choosing the segmentation $\hat{\mathcal{M}}$ that minimizes the posterior probability $P(\mathcal{M}^i | \mathcal{I}) = P(\mathcal{I} | \mathcal{M}^i)P(\mathcal{M}^i) / P(\mathcal{I})$ as

$$\hat{\mathcal{M}} = \arg \max_{\mathcal{M}^i} P(\mathcal{I} | \mathcal{M}^i)P(\mathcal{M}^i), \quad (1)$$

noting that $P(\mathcal{I})$ is a constant term. If optimal descriptive languages for a segmentation $\mathcal{L}_{\mathcal{M}}$, and the image given the segmentation $\mathcal{L}_{\mathcal{I}|\mathcal{M}}$, are available [31], the MAP criterion reduces to the MDL criterion given below:

$$\hat{\mathcal{M}} = \arg \min_{\mathcal{M}^i} \left| \mathcal{L}_{\mathcal{I}|\mathcal{M}}(\mathcal{I} | \mathcal{M}^i) \right| + \left| \mathcal{L}_{\mathcal{M}}(\mathcal{M}^i) \right|, \quad (2)$$

where $|\cdot|$ denotes the number of bits required to describe the data using $\mathcal{L}_{\mathcal{M}}$ and $\mathcal{L}_{\mathcal{I}|\mathcal{M}}$. Using optimal descriptive languages: $\left| \mathcal{L}_{\mathcal{I}|\mathcal{M}}(\mathcal{I} | \mathcal{M}^i) \right| = -\log_2 P(\mathcal{I} | \mathcal{M}^i)$, and $\left| \mathcal{L}_{\mathcal{M}}(\mathcal{M}^i) \right| = -\log_2 P(\mathcal{M}^i)$ bits, respectively [31]. The number of bits can be computed directly if the probability distribution $P(\mathcal{I} | \mathcal{M}^i)$ is known. Moreover, for each pixel, the pixel intensity probability distribution $P(\mathcal{I}(\mathbf{x}) | \mathcal{M}^i)$ can be replaced with $P(\mathcal{I}(\mathbf{x}) | \mathcal{M}^i, N(\mathbf{x}))$ to capture the inter-pixel correlations within a neighborhood $N(\mathbf{x})$ around the pixel \mathbf{x} [62]. The first term in (2) then becomes a summation

$$\left| \mathcal{L}_{\mathcal{I}|\mathcal{M}}(\mathcal{I}|\mathcal{M}^i) \right| = \sum_{\mathbf{x} \in \{\mathcal{F}^i, \mathcal{B}^i\}} -\log_2 P(\mathcal{I}(\mathbf{x})|\mathcal{M}^i, N(\mathbf{x})), \quad (3)$$

within the foreground \mathcal{F}^i and background \mathcal{B}^i regions of which a segmentation \mathcal{M}^i partitions the image into, i.e. $\mathcal{M}^i = \{\mathcal{F}^i, \mathcal{B}^i\}$.

In order to adapt the above approach to the immediate task of vessel/neurite segmentation, we need to specialize the term $P(\mathcal{I}(\mathbf{x})|\mathcal{M}, N(\mathbf{x}))$ in (3) for the vessel/neurite segmentations of interest since it is not provided by the MDL principle [29]. The term $P(\mathcal{I}(\mathbf{x})|\mathcal{M}^i, N(\mathbf{x}))$ is also a place where the vessel/neurite model \mathcal{G} around the neighborhood $N(\mathbf{x})$ of a pixel \mathbf{x} can be defined. For this, we adopt the multi-scale vesselness measure [27], denoted $\mathcal{V}_\sigma(\mathbf{x}) \in [0, 1]$, that measures the likelihood that a neighborhood of pixels centered at \mathbf{x} belong to a tube of size scale σ . It is based on the intensity-ridge modeling of vessels/neurites [5, 7, 8, 63], obtained from the scale-specific Hessian matrix:

$$H_\sigma(\mathbf{x}) = \sigma^\gamma \left[\mathcal{I}(\mathbf{x}) * \frac{\partial^2}{\partial \mathbf{x}^2} G_\sigma \right], \quad (4)$$

where G_σ is the Gaussian function with standard deviation σ , γ is the Lindeberg constant [64] for a family of scale-normalized derivatives, and “*” is the convolution operator. For a D-dimensional image, the eigenvalues of $H_\sigma(\mathbf{x})$, denoted λ_d , $d \leq D$, are ordered such that $|\lambda_d| \leq |\lambda_{d+1}|$. For two-dimensional (2-D) images, $\mathcal{V}_\sigma(\mathbf{x})$ is given by:

$$\mathcal{V}_\sigma(\mathbf{x}) = \begin{cases} 0, & \text{if } \lambda_2 > 0 \\ \exp\left(-\frac{R_B^2}{2\beta^2}\right) \left[1 - \exp\left(-\frac{S^2}{2c^2}\right) \right], & \end{cases} \quad (5)$$

where $R_B = |\lambda_1|/|\lambda_2|$ (inverse-likelihood of being on a tube) and $S = \sqrt{\sum_{d \leq D=2} \lambda_d^2}$ (image intensity contrast factor). The terms β and c in (5) are weighting parameters for R_B and S [27]. Using the vesselness measure to capture inter-pixel correlations, the first term in (2) now becomes:

$$\left| \mathcal{L}_{\mathcal{I}|\mathcal{M}}(\mathcal{I}|\mathcal{M}^i) \right| = \sum_{\mathbf{x} \in \{\mathcal{F}^i, \mathcal{B}^i\}} -\log_2 P(\mathcal{V}(\mathbf{x})). \quad (6)$$

It is possible to use other measures that capture vessel/neurite structure (e.g. [15, 25, 26]) although they are not explored in this paper.

Notice that the vesselness value in (5) increases with decreasing magnitude of R_B , effectively capturing the eigenvalues-shape associations for tube-like objects. This suggests that (5) can be modified accordingly for other basic geometrical models. Frangi *et al.* [27] have described approaches to adapt this method to other key geometrical models in biological images. Table I is a simplified summary linking key geometrical models and the corresponding eigenvalues.

For the second term in (2) a descriptive language $\mathcal{L}_{\mathcal{M}}$ has to be chosen. For the present work, the pixel-chain code suggested by Leclerc [31] has been adopted. Using this code, once the starting point of a chain of pixels (e.g. a vessel/neurite segment) is defined, the subsequent pixels in the chain are identified as one of the possible neighbors using a small number of bits. For example, in 2-D, only 3 bits are needed for the chained pixels (8 possible neighbors) instead of 32 bits each for the x and y coordinate locations.

At this point, the problem of image segmentation is ready to be wrapped into an optimization framework (Fig. 2b) using the MDL-criterion in (2) that trades off conciseness and coverage. Before proceeding, the users are given the optional ability to override/bias the tradeoff between conciseness and segmentation coverage using a universal parameter $\alpha \in [0,1]$. When $\alpha = 0.5$, the conciseness-coverage tradeoff is a balanced one. Overall, the segmentation quality metric q is a function of the image \mathcal{I} , segmentation algorithm parameter settings ξ , universal parameter α , and the neighborhood-based geometrical/intensity model \mathcal{G} , and is written as follows:

$$q(\mathcal{M}^i|\mathcal{I}, \xi^i, \alpha, \mathcal{G}) = \alpha \underbrace{\left| \mathcal{L}_{\mathcal{I}|\mathcal{M}}(\mathcal{I}|\mathcal{M}^i) \right|}_{\text{coverage}} + (1-\alpha) \underbrace{\left| \mathcal{L}_{\mathcal{M}}(\mathcal{M}^i) \right|}_{\text{conciseness}}, \quad (7)$$

using the coverage term as defined in (6) and the conciseness term with the pixel-chain code [31].

IV. RECURSIVE RANDOM SEARCH STRATEGY

Several considerations motivate the selection of Recursive Random Search (RRS), as a preferred strategy compared to other available alternatives. First, exhaustive search is time-prohibitive. Second, the objective function is not differentiable with respect to the parameter vector, mainly because the mapping itself is not differentiable. Third, for the image segmentation problems of interest, it is rational to seek approximate solutions within a defined time frame, rather than truly global optima. Fourth, it is common for segmentation software to have several irrelevant/ineffective settings for a given application, and search algorithms that are able to minimize the computational effort in such dimensions are preferable. Finally, we expect the search algorithm to be robust to minor noise-like fluctuations in the objective function. Interestingly, Ye *et al.* [47] developed this algorithm motivated by similar parameter spaces encountered in computer networking – specifically, automatic and dynamic configuration of network components to maximize network throughput.

As indicated by the name, the RRS algorithm is based on random sampling. This algorithm searches the parameter space in two recursive steps: exploration and exploitation, respectively. The exploration step examines the macroscopic features of the objective function (e.g., globally convex or “big valleys” structure [15]) and attempts to identify promising areas in the parameter space Ω that are subsequently “exploited” intensively by the second step, called the exploitation step. For the random sampling, a uniform distribution over Ω is used. This has been shown to be the simplest search technique for similar non-linear problems, and is widely used [47, 55, 56, 65]. It has been shown to be more efficient for exploring high-dimensional parameter spaces compared to deterministic exploration methods [47, 66], and can be shown to converge to the global optima [67].

We show below that random sampling is in fact very efficient in its initial steps and only starts to become inefficient in the later sampling steps. Given a measurable objective function $q(\xi)$ over the parameter space Ω , we can define the distribution of objective function values for some $q_0 \in [q_{\min}, q_{\max}]$ as $\phi_{\Omega}(q_0) = m(\{\xi \in \Omega \mid q(\xi) \leq q_0\}) / m(\Omega)$, where $m(\cdot)$ is the Lebesgue measure. Hence, the distribution

function $\phi_{\Omega}(q_0)$ represents the portion of the points in the parameter space whose objective function values are smaller than a certain level q_0 . Furthermore, it has a maximum value of 1 when $q_0 = q_{\max}$, and has minimum value(s) of $m(\hat{\xi})/m(\Omega)$ where $\hat{\xi}$ is (the set of) global optimum(optima). Without loss of generality, assume that $q(\xi)$ is a continuous function and $m(\{\xi \in \Omega | q(\xi) = q_0\}) = 0, \forall q_0 \in [q_{\min}, q_{\max}]$.

Assuming a $q_r \in [q_{\min}, q_{\max}]$ such that $\phi_{\Omega}(q_r) = r, r \in [0, 1]$, an r -percentile subspace $\mathcal{S}_{\Omega}(r)$ in the parameter space can be defined as $\mathcal{S}_{\Omega}(r) = \{\xi \in \Omega | q(\xi) \leq q_r\}$. Note that $\mathcal{S}_{\Omega}(1)$ is just the whole parameter space and $\lim_{\delta \rightarrow 0} \mathcal{S}_{\Omega}(\delta)$ converges to the global optima. Suppose the sample sequence generated by n steps of random sampling is $\{\xi\}_{i=1}^n$ and $\xi^{(i)}$ is the one with the minimum objective function value, then the probability of $\xi^{(i)}$ in $\mathcal{S}_{\Omega}(r)$ is given by $P(\{\xi^{(i)} \in \mathcal{S}_{\Omega}(r)\}) = 1 - (1 - r)^n = p$. Stated in another way, the value of r for which $\xi^{(i)}$ will be reached with probability p is given by $r = 1 - (1 - p)^{1/n}$.

For any $0 < p < 1$, r will tend to 0 with increasing n , implying that random sampling will converge to the global optima with increasing numbers of samples. Since r decreases exponentially with increasing n , the efficiency of random sampling is high at initial samples but falls sharply at later samples. This observation led to the idea of restarting the sampling before its efficiency drops off [47], either by moving or resizing the sample space according to sample history.

Specifically, RRS performs exploitation in two iterative steps: (i) random sampling within the current space, and (ii) realign or shrink. As illustrated in Fig. 3a, after drawing certain number of random samples (we used 7 in this paper) within the current space \mathcal{S}_1 , if a superior sample ξ_2 is found, then \mathcal{S}_1 centered at the current sample ξ_1 is realigned (moved) to the sample space \mathcal{S}_2 . If no better sample is found during the random sampling, the parameter space \mathcal{S}_1 is shrunk to \mathcal{S}_3 instead of realigning to \mathcal{S}_2 as shown in Fig. 3b.

The strategy for limiting the exploitation step to promising subspaces is based on identifying an

r -percentile subspace for exploitation, as described above. In this way, most trivial subspaces will be excluded from exploitation, improving the overall efficiency of the search. In contrast, algorithms such as multi-start [65], do not distinguish between subspaces and hence may waste time in trivial areas.

The RRS is efficient at handling an objective function with a subset of ineffective parameters [47] because random samples maintain a uniform distribution within the subspace composed of only the effective parameters, minimizing the computational effort invested on negligible parameters. In contrast, local search methods are affected by unimportant parameters because of their high dependency on dimensionality of the search space. For more details, the interested reader is referred to [47].

V. EXPERIMENTAL RESULTS AND EXAMPLES

This section provides a series of 2-D examples of progressively increasing complexity, starting with the simplest case of segmentation by global image thresholding. It is followed by a neuron tracing algorithm [1, 3] in which just two parameters out of eight are optimized, and concluded with a full eight-dimensional parameter search. In all examples, $\alpha = 0.5$ is chosen for pure MDL-balanced optimization. Also in all examples: (i) the size scales are obtained from the image content; and, (ii) the parameters for the vesselness measure are set to the values published in [27].

To evaluate the segmentation quality metric q using the description length in (6) the probability distribution function (PDF) of the vesselness values were estimated using 20 ground truth segmentations from the Digital Retinal Images for Vessel Extraction (DRIVE) database [25] and used in generating all presented results. Fig. 4 displays empirical and best-fit PDF of the vesselness values at the background regions \mathcal{B} in Panel (a) and at the foreground regions \mathcal{F} in Panel (b). Ranked by the Kolmogorov-Smirnov (KS) test statistic, the exponential distribution for \mathcal{B} (KS value 0.27) and the generalized-beta distribution for \mathcal{F} (KS value 0.05) were determined to be the best fit out of 15 distributions considered. The parameters of the best-fitted distributions were obtained using maximum-likelihood estimation.

Example #1: This example is intended to illustrate the methodology in a trivial and readily-understood context – global intensity thresholding [68]. A global intensity threshold τ is applied to

images containing tube-like structures, and the goal is to find the optimal value $\hat{\tau}$ that yields the optimal segmentation $\hat{\mathcal{M}}$. For objects brighter than the background, the segmentation function is given by:

$$f(\mathcal{I}(\mathbf{x}), \xi) = \begin{cases} \mathbf{x} \in \mathcal{F} & \text{if } \mathcal{I}(\mathbf{x}) \geq \tau \\ \mathbf{x} \in \mathcal{B} & \text{otherwise} \end{cases}. \quad (8)$$

For 8-bit grayscale images, $\mathcal{I}(\mathbf{x}) \in [0, 255]$, the global intensity threshold $\xi = \tau \in [0, 255]$ is a one-dimensional parameter vector in the parameter space $\Omega \in \mathbb{Z}^1$. Fig. 5 shows the results of applying the proposed methodology to this case. Panel (a) shows an image of neuronal dendrites captured by fluorescence microscopy. The vesselness measure $\mathcal{V}(\mathbf{x})$ is displayed in Panel (b). Panel (c) is a plot of the objective function q versus the threshold value τ . The optimal segmentation $\hat{\mathcal{M}}$ (using the optimal threshold value $\hat{\tau} = 41$) is shown in Panel (d).

Example #2: In this example, we show the use of the proposed methodology to choose the optimal parameters $\hat{\xi}$ for an automated neuron tracing algorithm [1, 3]. The parameter settings for this algorithm can be combined into a vector as follows (Appendix):

$$\xi = (g \quad L_{\min} \quad L_{\max} \quad n_{\text{shift}} \quad n_{\text{rotate}} \quad s_{\max} \quad \tau_c \quad \nu).$$

They are summarized in Table II, along with their default values. Note that the traces are not merged for these examples since the segments are merged after tracing by the tracing software.

Fig. 6 shows the result of an exhaustive search for just two parameters, grid spacing g in the range $[10, 30]$, and contrast threshold multiplier τ_c in the range $[1, 10]$ with other parameters set at default values. Panel (a) shows the input image containing fluorescently-labeled neurites imaged using a multi-photon microscope. Panel (b) shows the computed vesselness values. Panel (c) displays the entire optimization objective function q versus g and τ_c . Panel (d) displays the traces obtained using the default parameter values ($g = 15, \tau_c = 3$). The worst under-segmentation ($g = 26, \tau_c = 10$), is displayed in panel (e). Panel (f) displays the worst over-segmentation ($g = 10, \tau_c = 1$). The optimal segmentation

($g = 21, \tau_c = 8$) is displayed in panel (g). Since only two parameters are being searched here, it is feasible to search exhaustively. These two parameters are related directly to the initial sampling of the image and the stopping criteria of the tracing algorithm. They are chosen to illustrate the effect of these aspects of the tracing algorithm on trace conciseness and coverage.

Example #3: This example shows the search in the full eight-dimensional parameter space of the tracing algorithm, using at most 1000 RRS trials. For this example, 40 test images of human retinas (with ground truth), and 183 images of neurites were gathered from four sources (Table III). For the retinal images, the pixel-wise agreement to the ground truth was also computed. Improvements in description lengths and agreement with the ground truth were found to be strongly correlated ($\rho = 0.78$), and statistically significant ($p < 0.0005$ to reject the hypothesis $\rho = 0$). From this point onwards, all reported improvements in this section are in terms of the segmentation quality metric q compared to using the algorithm's default parameter settings (Table II).

Fig. 7 displays the applications of the proposed method to a human retinal fundus image shown in panel (a) and to images of cultured neurons in panels (b)-(d). Traces using default settings are shown in panels (e)-(h). Traces using automatically-selected settings using 1000 RRS trials are shown in panels (i) through (l). The quality improvement is 4% for the retina image in panel (a), 6% for the neuron image in panel (b), 7% for the neuron image in panel (c), and 38% for the neuron image on the micro-fabricated surface in panel (d).

Table III summarizes the results for all 223 test images. The first column lists the image source followed by the number of images in the second column. The third column shows the improvements in q when the optimal parameter settings are obtained for each image. The fourth column shows the improvements when optimal settings for the first image from the same source are applied to the rest of the images. The reported improvements are all statistically significant ($p < 0.0005$) as concluded from paired t -tests on all test images.

Fig. 8 graphically displays the segmentation quality improvements on the batch of images from

the Synaptic Distribution Study [69] as summarized in Table III. The fourth image from this batch is shown in Fig. 7b. The shaded bars show the percentage improvements in the segmentation quality metric when optimal parameter settings are computed for each image. Twelve images were found to share the same settings after 1000 RRS trials. The blank bars show the percentage improvements when settings are optimized for just one randomly selected image, and then applied to the rest of the images in the batch.

The execution time is dependent on the time for one RRS trial, i.e., one run of the segmentation algorithm. For this exploratory algorithm, the execution time scales with image content [3]. As such, execution times for 1000 RRS trials to obtain the optimal parameter settings vary from 12 minutes per image on average from the DRIVE database [25] to 53 minutes on average for images from the Synaptic Distribution Study [69] on a 2GHz AMD Opteron processor.

The performance of the RRS algorithm is plotted in Fig. 9, displaying the segmentation quality improvement in percentage relative to using default segmentation algorithm parameter settings, on average, for all 223 test images. The average improvement relative to default settings increases only by 0.22% beyond 500 RRS trials up to 1000 RRS trials. This plot also illustrates the high efficiency of RRS during its exploration of the global parameter space. Furthermore, it shows that the default parameter settings are very unsuitable for the majority of the test images, especially from the neurite outgrowth directionality study [28] (see Table III). The minimum number of RRS trials is determined by the confidence-level of finding the optimal value within the global sample space, i.e., during its exploration step. For the 99% confidence-level used for all presented examples, RRS needs 44 trials [47] before it can begin identifying the promising subspaces for the exploitation step.

VI. CONCLUSIONS AND DISCUSSION

We have demonstrated the practicality of automatically tuning complex segmentation algorithms, using automatic segmentation quality assessment and global optimization, guided by the MDL principle. The proposed approach can greatly simplify the external interface of segmentation software packages, enable adaptation across large image batches from bioassays, and reduce the need for expensive technical

support. On batches of similar images, we have demonstrated that significant improvements can still be gained when the automated parameter selection method is performed on a single representative image (or perhaps, a modest subset) and the obtained parameter settings are applied to the rest of the images. This yields a better operating point for the segmentation algorithm compared to application-independent default values.

The proposed methodology is fully automatic and self-contained, and free of user interactions such as in reinforcement-learning segmentation systems [46]. The core idea of trading off segmentation conciseness and segmentation coverage is extensible to other applications and other geometrical models, which remains as future work. The optional universal parameter α allows a user to bias the tradeoff. The modularity of the proposed framework allows insertion of alternative segmentation algorithms and/or global optimization algorithms, as long as the interfaces between modules are maintained [70]. Algorithms for segmenting other key biological objects types such as blobs [71, 72] would require matching quality measures.

APPENDIX: A BRIEF DESCRIPTION OF THE EXPLORATORY TRACING ALGORITHM

The tracing algorithm [1, 3] models tube-like biological structures as piecewise-linear generalized cylinder segments. In 2-D, this reduces to finding a pair of almost-parallel edges (Fig. 10). To begin tracing, seed points are found by searching for local maxima along rectangular grids g pixels apart and are validated using the same generalized cylinder model.

Then, at each tracing iteration j , two boundary points $\{\mathbf{b}_L^j, \mathbf{b}_R^j\}$ corresponding to the left and right tube boundaries are each found using directional correlation kernels called templates. The center point \mathbf{c}^j is simply defined as the center of these boundary points. Each template consists of linearly stacked 1-D edge-detector kernels of the form $(-1, -2, 0, +2, +1)^T$ anchored at the image point \mathbf{b}^j along a particular direction \mathbf{u}^j . The edge-strengths from each 1-D edge detector kernel r are averaged through the entire template length $l \in L$, using median statistics [73] for robustness. The set

$L = [L_{\min}, L_{\max}]$ contains all template lengths. The correlation between the templates and the image is called the “template response”, denoted R , as below:

$$R(\mathbf{b}^j, \mathbf{u}^j, L) = \arg \max_{l \in L} \left\{ \text{median}_{t=1,2,\dots,l} \left\{ r(\mathbf{b}^j + t\mathbf{u}^j) \right\} \right\}.$$

Each boundary point corresponds to the maximal response template parameters $\{\mathbf{b}^j, \mathbf{u}^j, l^j\}$:

$$(\mathbf{b}^j, \mathbf{u}^j, l^j) = \arg \max_{\{(\mathbf{b}, \mathbf{u}, l) \mid \mathbf{b} = \mathbf{c}^j + m\mathbf{u}_{\perp}, m=1, \dots, \frac{M}{2}, \mathbf{u} \in \mathbf{U}, l \in L\}} R(\mathbf{b}, \mathbf{u}, L),$$

where \mathbf{U} is the set of unit vectors along directions in the neighborhood of \mathbf{u}^j . The user parameter M is the radius of the widest expected vasculature. Each template is elongated, shifted from \mathbf{c}^j , and rotated to find the corresponding boundary points. To save computation, the template is only shifted in a neighborhood n_{shift} of previously calculated width at iteration $j-1$ and rotated in a neighborhood n_{rotate} around previously calculated tracing direction \mathbf{u}^{j-1} . The estimate of the next center point $\tilde{\mathbf{c}}^{j+1}$ is computed by scaling \mathbf{u}^j with the adaptive step-size s^j . This estimate is finalized to \mathbf{c}^{j+1} in the next iteration after the tube boundaries are found using the templates. The same process is repeated until a stopping criterion containing a contrast-based threshold multiplier τ_c is met ν consecutive times. The interested reader is referred to [1, 3] for details of the algorithm.

ACKNOWLEDGMENT

We thank colleagues O. Al-Kofahi, W. Shain, J. Turner, G. Banker, G. Lin, J. R. Glaser, E. Glaser, and J. Sprenger for test image contributions and discussions. We also thank M. Goldbaum *et al.* and M. Niemeijer *et al.* for their publicly-available image and ground truth segmentation databases.

REFERENCES

- [1] M.-A. Abdul-Karim, K. Al-Kofahi, E. B. Brown, R. K. Jain, and B. Roysam, "Automated tracing and change analysis of angiogenic vasculature from in vivo multiphoton confocal image time series," *Microvasc. Res.*, vol. 66, pp. 113-125, 2003.

- [2] K. A. Al-Kofahi, A. Can, S. Lasek, D. H. Szarowski, N. Dowell-Mesfin, W. Shain, J. N. Turner, and B. Roysam, "Median-based robust algorithms for tracing neurons from noisy confocal microscope images," *IEEE Trans. Inform. Technol. Biomed.*, vol. 7, pp. 302-317, 2003.
- [3] K. A. Al-Kofahi, S. Lasek, D. H. Szarowski, C. J. Pace, G. Nagy, J. N. Turner, and B. Roysam, "Rapid automated three-dimensional tracing of neurons from confocal image stacks," *IEEE Trans. Inform. Technol. Biomed.*, vol. 6, pp. 171-187, 2002.
- [4] W. He, T. A. Hamilton, A. R. Cohen, T. J. Holmes, C. Pace, D. H. Szarowski, J. N. Turner, and B. Roysam, "Automated three-dimensional tracing of neurons in confocal and brightfield images," *Microsc. Microanal.*, vol. 9, pp. 296-310, 2003.
- [5] S. R. Aylward and E. Bullitt, "Initialization, noise, singularities, and scale in height ridge traversal for tubular object centerline extraction," *IEEE Trans. Med. Imag.*, vol. 21, pp. 61-75, 2002.
- [6] I. Y. Koh, W. B. Lindquist, K. Zito, E. A. Nimchinsky, and K. Svoboda, "An image analysis algorithm for dendritic spines," *Neural Comput.*, vol. 14, pp. 1283-310, 2002.
- [7] E. Meijering, M. Jacob, J. C. Sarria, P. Steiner, H. Hirling, and M. Unser, "Design and validation of a tool for neurite tracing and analysis in fluorescence microscopy images," *Cytometry*, vol. 58A, pp. 167-76, 2004.
- [8] G. J. Streekstra and J. van Pelt, "Analysis of tubular structures in three-dimensional confocal images," *Network*, vol. 13, pp. 381-95, 2002.
- [9] C. M. Weaver, P. R. Hof, S. L. Wearne, and W. B. Lindquist, "Automated algorithms for multiscale morphometry of neuronal dendrites," *Neural Comput*, vol. 16, pp. 1353-83, 2004.
- [10] A. Can, H. Shen, J. N. Turner, H. L. Tanenbaum, and B. Roysam, "Rapid automated tracing and feature extraction from retinal fundus images using direct exploratory algorithms," *IEEE Trans. Inform. Technol. Biomed.*, vol. 3, pp. 125-138, 1999.
- [11] L. M. Lorigo, O. D. Faugeras, W. E. Grimson, R. Keriven, R. Kikinis, A. Nabavi, and C. F. Westin, "CURVES: Curve evolution for vessel segmentation," *Med. Image Anal.*, vol. 5, pp. 195-206, 2001.

- [12] M. Maddah, A. Afzali-Kusha, and H. Soltanian-Zadeh, "Efficient center-line extraction for quantification of vessels in confocal microscopy images," *Med. Phys.*, vol. 30, pp. 204-11, 2003.
- [13] X. Jiang and D. Mojon, "Adaptive local thresholding by verification-based multithreshold probing with application to vessel detection in retinal images," *IEEE Trans. Pattern Anal. Machine Intell.*, vol. 25, pp. 131-137, 2003.
- [14] M. A. T. L. Figueiredo, J.M.N., "A nonsmoothing approach to the estimation of vessel contours in angiograms," *IEEE Trans. Med. Imag.*, vol. 14, pp. 162-172, 1995.
- [15] S. C. Chaudhuri, S.; Katz, N.; Nelson, M.; Goldbaum, M., "Detection of blood vessels in retinal images using two-dimensional matched filters," *IEEE Trans. Med. Imag.*, vol. 8, pp. 263-269, 1989.
- [16] L. C. Gang, O.; Krishnan, S.M., "Detection and measurement of retinal vessels in fundus images using amplitude modified second-order Gaussian filter," *IEEE Trans. Biomed. Eng.*, vol. 49, pp. 168-172, 2002.
- [17] W. E. S. Higgins, W.J.T.; Karwoski, R.A.; Ritman, E.L., "System for analyzing high-resolution three-dimensional coronary angiograms," *IEEE Trans. Med. Imag.*, vol. 15, pp. 377-385, 1996.
- [18] J. Lowell, A. Hunter, D. Steel, A. Basu, R. Ryder, and R. L. Kennedy, "Measurement of retinal vessel widths from fundus images based on 2-D modeling," *IEEE Trans. Med. Imag.*, vol. 23, pp. 1196-1204, 2004.
- [19] J. Chen and A. A. Amini, "Quantifying 3-D vascular structures in MRA images using hybrid PDE and geometric deformable models," *IEEE Trans. Med. Imag.*, vol. 23, pp. 1251-1262, 2004.
- [20] N. Flasque, M. Desvignes, J. M. Constans, and M. Revenu, "Acquisition, segmentation and tracking of the cerebral vascular tree on 3D magnetic resonance angiography images," *Med. Image Anal.*, vol. 5, pp. 173-183, 2001.
- [21] C. Toumoulin, C. Boldak, J. L. Dillenseger, J. L. Coatrieux, and Y. Rolland, "Fast detection and characterization of vessels in very large 3-D data sets using geometrical moments," *IEEE Trans. Biomed. Eng.*, vol. 48, pp. 604-606, 2001.

- [22] F. K. H. Quek and C. Kirbas, "Vessel extraction in medical images by wave-propagation and traceback," *IEEE Trans. Med. Imag.*, vol. 20, pp. 117-131, 2001.
- [23] K. Bühler, P. Felkel, and A. La Cruz, "Geometric methods for vessel visualization and quantification - A survey," in *Geometric Modeling for Scientific Visualization*, G. Brunnett, B. Hamann, H. Muller, and L. Linsen, Eds. Heidelberg: Springer-Verlag, 2004, pp. 399-420.
- [24] O. Wink, W. J. Niessen, and M. A. Viergever, "Multiscale vessel tracking," *IEEE Trans. Med. Imag.*, vol. 23, pp. 130-133, 2004.
- [25] J. Staal, M. D. Abramoff, M. Niemeijer, M. A. Viergever, and B. van Ginneken, "Ridge-based vessel segmentation in color images of the retina," *IEEE Trans. Med. Imag.*, vol. 23, pp. 501, 2004.
- [26] A. D. K. Hoover, V.; Goldbaum, M., "Locating blood vessels in retinal images by piecewise threshold probing of a matched filter response," *IEEE Trans. Med. Imag.*, vol. 19, pp. 203-210, 2000.
- [27] A. F. Frangi, W. J. Niessen, K. L. Vincken, and M. A. Viergever, "Multiscale vessel enhancement filtering," *Lect. Notes Comput. Sc.*, vol. 1496, pp. 130-137, 1998.
- [28] N. M. Dowell-Mesfin, M.-A. Abdul-Karim, A. M. P. Turner, S. Schanz, H. G. Craighead, B. Roysam, J. N. Turner, and W. Shain, "Topographically modified surfaces affect orientation and growth of hippocampal neurons," *J. Neural Eng.*, pp. 78-90, 2004.
- [29] J. Rissanen, *Stochastic complexity in statistical inquiry*. Singapore: World Scientific, 1989.
- [30] A. Barron, J. Rissanen, and B. Yu, "The minimum description length principle in coding and modeling," *IEEE Trans. Inform. Theory*, vol. 44, pp. 2743-2760, 1998.
- [31] Y. G. Leclerc, "Constructing simple stable descriptions for image partitioning," *Int. J. Comput. Vision*, vol. 3, pp. 73-102, 1989.
- [32] M. Heath, S. Sarkar, T. Sanocki, and K. Bowyer, "Comparison of Edge Detectors: A Methodology and Initial Study," *Comput. Vis. Image Underst.*, vol. 69, pp. 38-54, 1998.

- [33] M. D. Heath, S. Sarkar, T. Sanocki, and K. W. Bowyer, "A robust visual method for assessing the relative performance of edge-detection algorithms," *IEEE Trans. Pattern Anal. Machine Intell.*, vol. 19, pp. 1338-1359, 1997.
- [34] M. C. Shin, D. B. Goldgof, and K. W. Bowyer, "Comparison of edge detector performance through use in an object recognition task," *Comput. Vis. Image Underst.*, vol. 84, pp. 160-178, 2001.
- [35] K. Bowyer, C. Kranenburg, and S. Dougherty, "Edge Detector Evaluation Using Empirical ROC Curves," *Comput. Vis. Image Underst.*, vol. 84, pp. 77-103, 2001.
- [36] Y. Yitzhaky and E. Peli, "A method for objective edge detection evaluation and detector parameter selection," *IEEE Trans. Pattern Anal. Machine Intell.*, vol. 25, pp. 1027-1033, 2003.
- [37] P. Meer and B. Georgescu, "Edge detection with embedded confidence," *IEEE Trans. Pattern Anal. Machine Intell.*, vol. 23, pp. 1351-1365, 2001.
- [38] W. H. H. J. Lunscher and M. P. Beddoes, "Optimal edge detector design.1. Parameter selection and noise effects," *IEEE Trans. Pattern Anal. Machine Intell.*, vol. 8, pp. 164-177, 1986.
- [39] D. Mumford and J. Shah, "Optimal approximations by piecewise smooth functions and associated variational-problems," *Commun. Pur. Appl. Math.*, vol. 42, pp. 577-685, 1989.
- [40] J.-M. Morel and S. Solimini, *Variational methods in image segmentation*. Boston: Birkh user, 1995.
- [41] V. Chalana and Y. Kim, "A methodology for evaluation of boundary detection algorithms on medical images," *IEEE Trans Med. Imag.*, vol. 16, pp. 642-652, 1997.
- [42] S. C. Zhu and A. Yuille, "Region competition: Unifying snakes, region growing, and Bayes/MDL for multiband image segmentation," *IEEE Trans. Pattern Anal. Machine Intell.*, vol. 18, pp. 884-900, 1996.
- [43] C. Alberola-Lopez, M. Martin-Fernandez, and J. Ruiz-Alzola, "Comments on: A methodology for evaluation of boundary detection algorithms on medical images," *Medical Imaging, IEEE Transactions on*, vol. 23, pp. 658-660, 2004.

- [44] S. K. Warfield, K. H. Zou, and W. M. Wells, "Simultaneous truth and performance level estimation (STAPLE): an algorithm for the validation of image segmentation," *IEEE Trans. Med. Imag.*, vol. 23, pp. 903-921, 2004.
- [45] J. Min, M. Powell, and K. W. Bowyer, "Automated performance evaluation of range image segmentation algorithms," *IEEE Trans. Syst., Man, Cybern. B*, vol. 34, pp. 263-271, 2004.
- [46] J. Peng and B. Bhanu, "Closed-loop object recognition using reinforcement learning," *IEEE Trans. Pattern Anal. Machine Intell.*, vol. 20, pp. 139-154, 1998.
- [47] T. Ye and S. Kalyanaraman, "Internet traffic engineering - A recursive random search algorithm for large-scale network parameter configuration," *ACM SIGMETRICS Perf. Eval. Rev.*, vol. 31, pp. 10, 2003.
- [48] M. Niemeijer, J. Staal, B. van Ginneken, M. Loog, and M. D. Abramoff, "Comparative study of retinal vessel segmentation methods on a new publicly available database [5370-69]," presented at Image Processing Conference, San Diego, Calif., 2004.
- [49] T. Kanungo, M. Y. Jaisimha, J. Palmer, and R. M. Haralick, "A methodology for quantitative performance evaluation of detection algorithms," *IEEE Trans. Image Processing*, vol. 4, pp. 1667-1674, 1995.
- [50] O. D. Trier and A. K. Jain, "Goal-directed evaluation of binarization methods," *IEEE Trans. Pattern Anal. Machine Intell.*, vol. 17, pp. 1191-1201, 1995.
- [51] Y. J. Zhang, "A survey on evaluation methods for image segmentation," *Pattern Recog.*, vol. 29, pp. 1335-1346, 1996.
- [52] A. Hammoude, "An empirical parameter selection method for endocardial border identification algorithms," *Comput. Med. Imag. Grap.*, vol. 25, pp. 33-45, 2001.
- [53] M. Mitchell, *An introduction to genetic algorithms*. Cambridge, Mass.: MIT Press, 1996.
- [54] S. Kirkpatrick, C. D. Gelatt, and M. P. Vecchi, "Optimization by simulated annealing," *Science*, vol. 220, pp. 671-680, 1983.

- [55] W. L. Price, "Global optimization by controlled random search," *J. Optimiz. Theory App.*, vol. 40, pp. 333-348, 1983.
- [56] A. H. Kan and G. T. Timmer, "Stochastic global optimization methods.2. Multi level methods," *Math. Program.*, vol. 39, pp. 57-78, 1987.
- [57] J. E. Falk and R. M. Soland, "Algorithm for separable nonconvex programming problems," *Manage. Sci.*, vol. 15, pp. 550-569, 1969.
- [58] L. Armijo, "Minimization of functions having lipschitz continuous first partial derivatives," *Pac. J. Math.*, vol. 16, pp. 1-8, 1966.
- [59] R. Hooke and T. A. Jeeves, "Direct search solution of numerical and statistical problems," *J. ACM*, vol. 8, pp. 212-218, 1961.
- [60] N. J. Radcliffe and P. D. Surry, "Fundamental limitations on search algorithms: Evolutionary computing in perspective," *Lect. Notes Comput. Sc.*, vol. 1000, pp. 275-291, 1995.
- [61] D. H. Wolpert and W. G. Macready, "No free lunch theorems for optimization," *IEEE Trans. Evol. Comput.*, vol. 1, pp. 67-82, 1997.
- [62] J. Besag, "On the statistical-analysis of dirty pictures," *J. Roy. Stat. Soc. B. Met.*, vol. 48, pp. 259-302, 1986.
- [63] D. Eberly, *Ridges in image and data analysis*. Boston: Kluwer Academic Publishers, 1996.
- [64] T. Lindeberg, "Edge detection and ridge detection with automatic scale selection," *Int. J. Comput. Vision*, vol. 30, pp. 117, 1998.
- [65] A. Törn and A. Zhilinskas, *Global optimization*. Berlin; New York: Springer-Verlag, 1989.
- [66] B. Xi, Z. Liu, M. Raghavachari, C. H. Xia, and L. Zhang, "A smart hill-climbing algorithm for application server configuration," presented at The 13th Int. Conf. on WWW, New York, 2004.
- [67] R. Y. Rubinstein, *Simulation and the monte carlo method*. New York: Wiley, 1981.
- [68] P. K. Sahoo, S. Soltani, A. K. C. Wong, and Y. C. Chen, "A survey of thresholding techniques," *CVGIP*, pp. 233-60, 1988.

- [69] H. Narasimha-Iyer, N. M. Dowell-Mesfin, M.-A. Abdul-Karim, B. Roysam, J. N. Turner, and W. Shain, "Associative Multiple-Label Image Analysis Method for Synapse Identification in Neuronal Cultures: Application to Comparative Analysis of Synapse Formation Efficiency & Distribution on Smooth and Topographically Modified Surfaces," presented at Microscopy and Microanalysis, Honolulu, 2005.
- [70] E. Gamma, *Design patterns: elements of reusable object-oriented software*. Reading: Addison-Wesley, 1995.
- [71] G. Lin, U. Adiga, K. Olson, J. F. Guzowski, C. A. Barnes, and B. Roysam, "A hybrid 3D watershed algorithm incorporating gradient cues and object models for automatic segmentation of nuclei in confocal image stacks," *Cytometry*, vol. 56A, pp. 23-36, 2003.
- [72] C. Ortiz De Solorzano, E. Garcia Rodriguez, A. Jones, D. Pinkel, J. W. Gray, D. Sudar, and S. J. Lockett, "Segmentation of confocal microscope images of cell nuclei in thick tissue sections," *J Microsc*, vol. 193, pp. 212-226, 1999.
- [73] P. J. Huber, *Robust statistics*. New York: Wiley, 1981.

TABLE I

Geometrical Model \mathcal{G}	λ_1	λ_2	λ_3
Tube-like	≈ 0	$\ll 0$	$\ll 0$
Blob-like	$\ll 0$	$\ll 0$	$\ll 0$
Plate-like	≈ 0	≈ 0	$\ll 0$

The eigenvalues of the Hessian matrix indicate common geometrical models in biological cell and tissue-level imagery, as shown [27]. For dark objects on bright backgrounds, the signs are reversed. In 2-D, the first two eigenvalues λ_1 and λ_2 are used and plate-like structures cannot be resolved. All three eigenvalues are used in 3-D.

TABLE II

Parameter	Range	Default Value	Constraint on Values
Grid spacing g	10 – 30	15	divisible by 5 ^a
Minimum template length L_{\min}	8 – 20	10	$L_{\min} \leq L_{\max}$
Maximum template length L_{\max}	8 – 30	18	$L_{\min} \leq L_{\max}$
Relative shift distance n_{shift}	2 – 10	2	none
Directional degree of freedom n_{rotate}	3 – 7	7	odd-numbered
Maximum step size s_{\max}	3 – 10	8	$s_{\max} \leq L_{\min}$
Contrast threshold multiplier τ_c	1 – 10	3	none
Maximum allowed stopping violations ν	1 – 10	1	none

The components of the parameter vector $\xi \in \mathbb{Z}^8$, their respective ranges, default values, and constraints on their values for the tracing algorithm.

^aThis constraint is omitted for generating the results and the optimization landscape in Fig. 6.

TABLE III

Image Source and Reference	Number of Images	Improvement in quality q with 1000 RRS iterations, compared to default settings	
		Improvement when each image is optimized (%)	Improvement when just one image is optimized (%)
Directionality of Neurite Outgrowth Study (Neuron) [28]	154	21.3	18.5
The STARE Project (Retina) [26]	20	4.7	1.3
The DRIVE Database (Retina) [25]	20	9.0	4.1
Synaptic Distribution Study (Neuron) [69]	29	10.9	10.0

Summary of experimental results with 223 images from four sources. The first two columns list the image sources, and number of images. For all experiments, 1000 RRS iterations were used, and an 8-dimensional parameter space was searched. The third column shows the improvements in the segmentation quality metric q when optimal parameter settings are computed for each image. The fourth column shows the improvements when settings are optimized for just one randomly selected image, and then applied to the rest of the images in the batch.

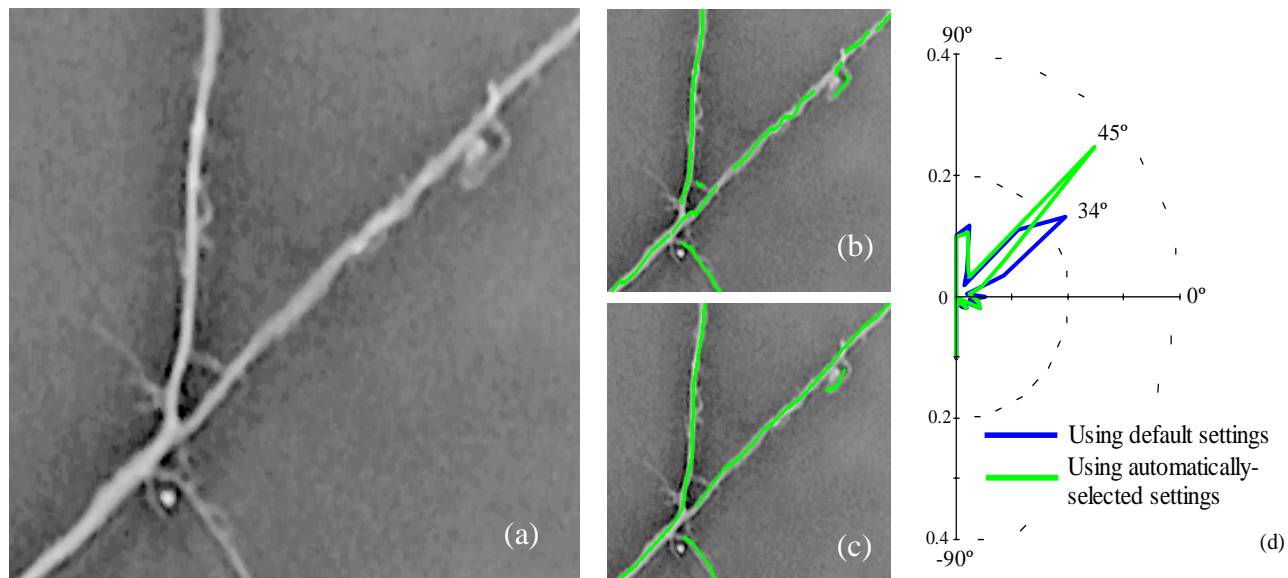


Fig. 1. Optimal tracing settings lead to more accurate measurements. (a) A phase contrast image of cultured neurites grown on an imprinted surface with known orientations of 45° and 90° . (b) Automatically-generated traces using default settings. (c) Traces obtained with automatically selected parameters using the method presented in this paper. (d) The normalized angular histogram of measured segment orientations extracted from the automatically-generated traces. Note the correct peak at 45° obtained using automatically-selected settings vs. 34° using default settings. (Data courtesy: Dr. Gary Banker, OHSU).

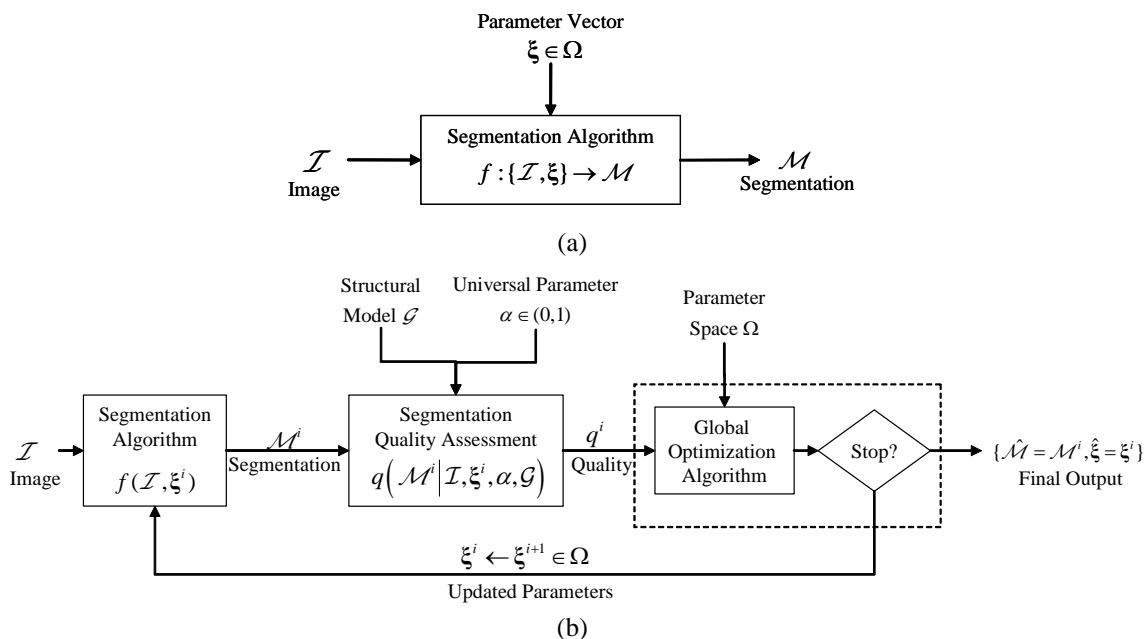


Fig. 2. Illustrates the proposed self-optimizing image segmentation approach. Panel (a) shows a traditional segmentation algorithm in which the parameter settings ξ are set empirically for each input image \mathcal{I} . Panel (b) illustrates the proposed method in which a global optimization algorithm efficiently explores the parameter space Ω driven by a segmentation quality assessment value based on trading off conciseness of the segmentation vs. its coverage. The user optionally specifies a single universal parameter to override the tradeoff.

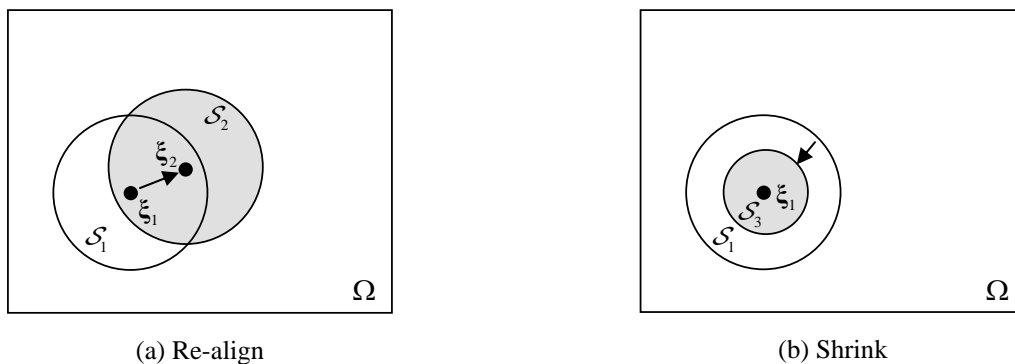


Fig. 3. Venn diagrams illustrating the re-align and shrink operations in the exploitation step of the recursive random search algorithm (RRS). The current sample is denoted ξ_1 , and the local exploitation subspace is depicted as a un-shaded circle around it. After drawing a certain number of random samples within the current space \mathcal{S}_1 , if a better sample ξ_2 is found, then the search is re-aligned to the sample space \mathcal{S}_2 . If no better sample is found during the random sampling, the parameter space \mathcal{S}_1 is shrunk to \mathcal{S}_3 instead of realigning to \mathcal{S}_2 .

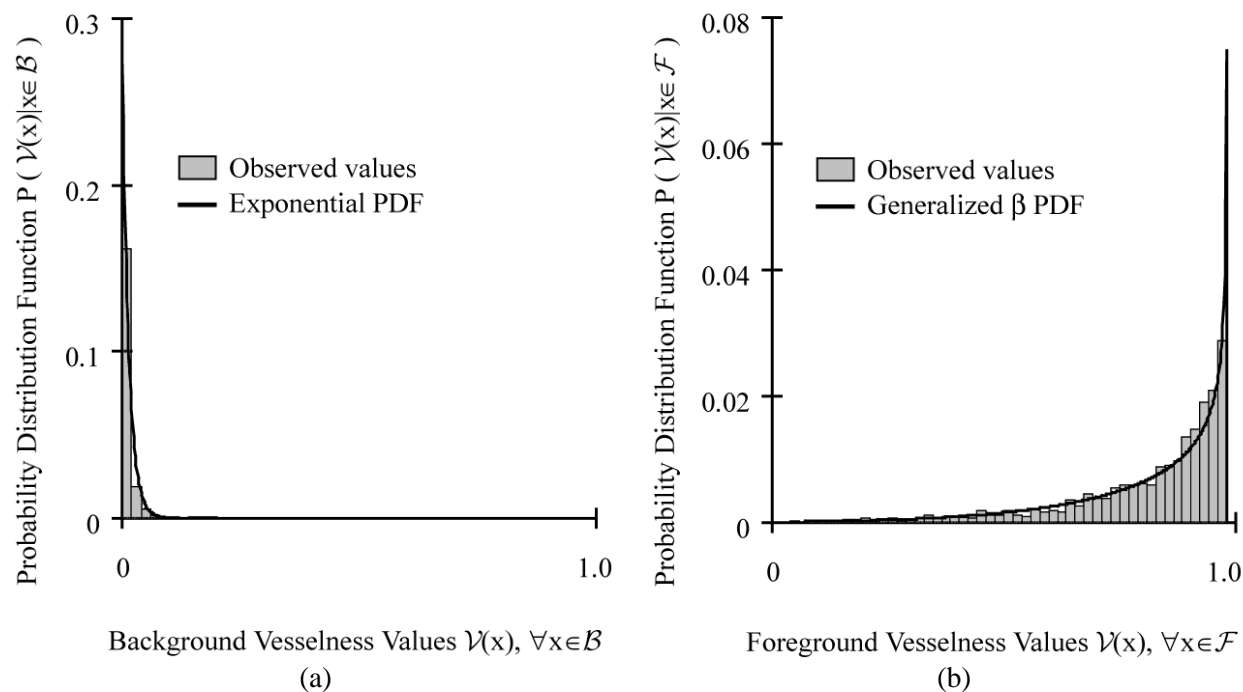


Fig. 4. Displays empirical and best-fit probability distribution function (PDF) of the vesselness values at the background regions \mathcal{B} in Panel (a) and at the foreground regions \mathcal{F} in Panel (b). Ranked by the Kolmogorov-Smirnov (KS) test statistic, the exponential distribution for \mathcal{B} (KS value 0.27) and the generalized-beta distribution for \mathcal{F} (KS value 0.05) were determined to be the best fit out of 15 distributions considered. The parameters of the best-fitted distributions were obtained using maximum-likelihood estimation.

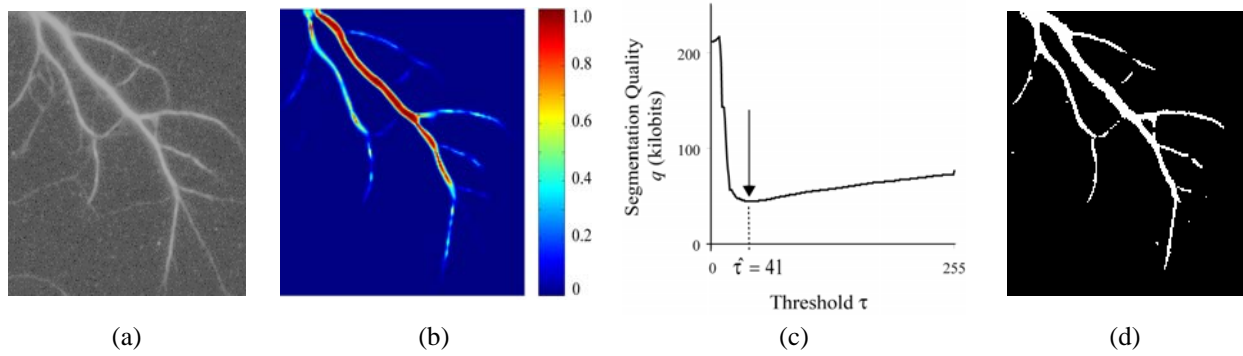


Fig. 5. Trivial automatic thresholding example illustrating the behavior of the segmentation quality metric q . (a) Image of a fluorescently labeled neurite captured by a widefield microscope. (b) The multi-scale vesseness measure. (c) Plot of the metric q against the threshold τ value. (c) The optimal segmentation $\hat{\mathcal{M}}$ using $\hat{\tau} = 41$.

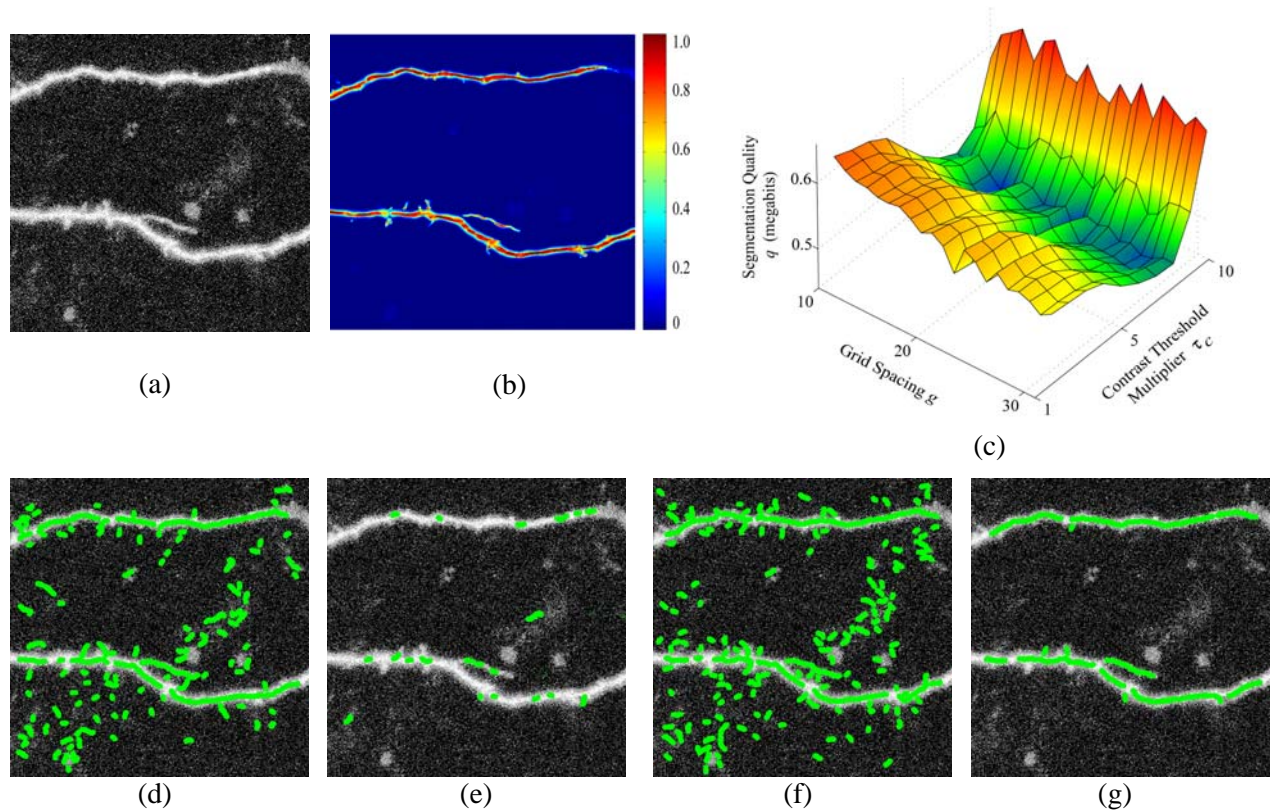


Fig. 6. An example varying just two parameters, $g \in [10, 30]$ and $\tau_c \in [1, 10]$, with others fixed at default values (Table II). Panel (a) shows a multi-photon microscope image of fluorescently-labeled neurites. Panel (b) displays the vesseness measure. Panel (c) shows the non-trivial optimization landscape. (d) Using the default parameter values ($g = 15, \tau_c = 3$). (e) The worst under-segmentation ($g = 26, \tau_c = 10$). (f) The worst over-segmentation ($g = 10, \tau_c = 1$). (g) The optimal segmentation ($g = 21, \tau_c = 8$).

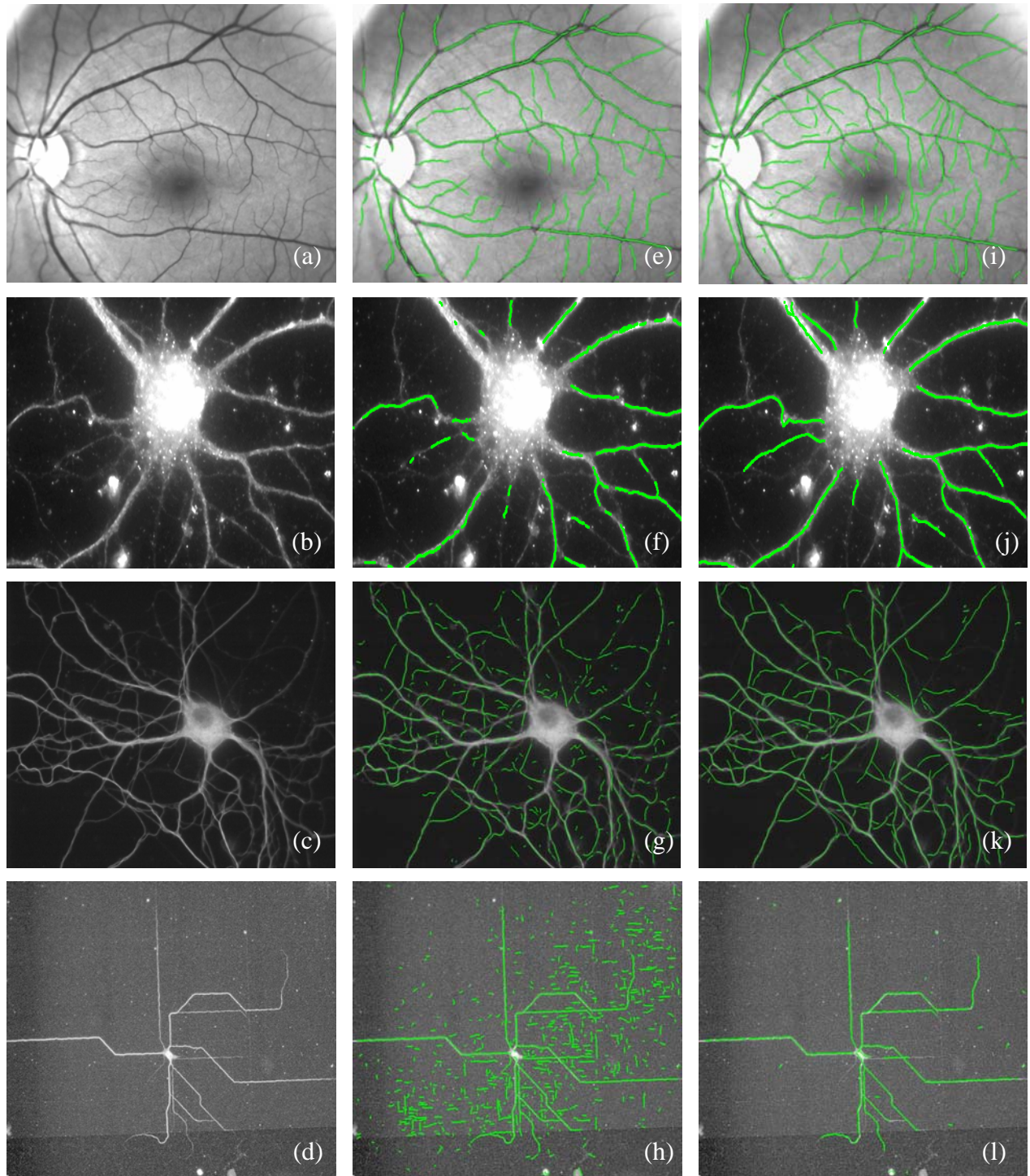


Fig. 7. Illustrating applications of the proposed method to: (a) a human retinal fundus image; (b)-(d) images of cultured neurons. Default traces are shown in panels (e) through (h). Traces using automatically-selected settings using 1000 RRS trials are shown in panels (i) through (l). The quality improvement is 4% for the retina image in panel (a), 6% for the neuron image in panel (b), 7% for the neuron image in panel (c), and 38% for the neuron image on the micro-fabricated surface in panel (d).

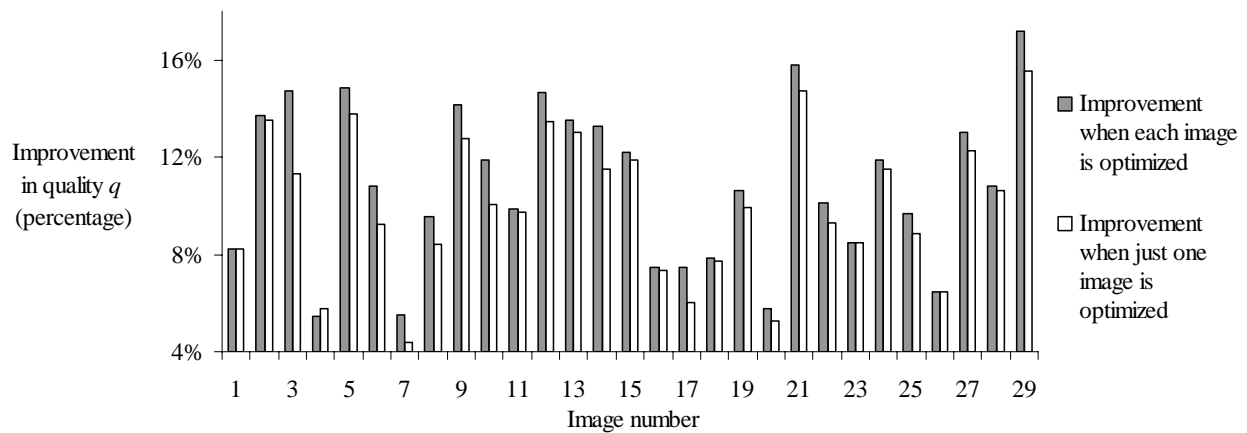


Fig. 8. Displays the segmentation quality improvements on the batch of images from the Synaptic Distribution Study [69] as summarized in Table III. The fourth image from this batch is shown in Fig. 7b. The shaded bars show the percentage improvements in the segmentation quality metric when optimal parameter settings are computed for each image. The blank bars show the percentage improvements when settings are optimized for just one randomly selected image, and then applied to the rest of the images in the batch.

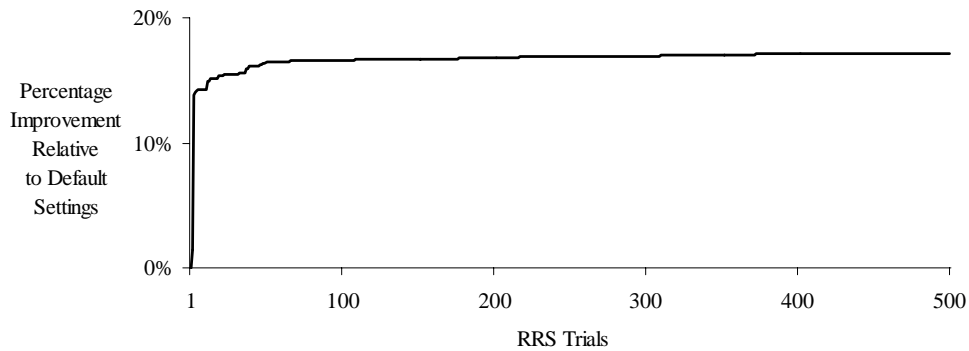


Fig. 9. Average percentage improvement in segmentation quality for all 223 test images (Table III). This plot illustrates the high efficiency of RRS during its early exploration of the global parameter space. The improvement between 500 and 1000 RRS trials is only 0.22%.

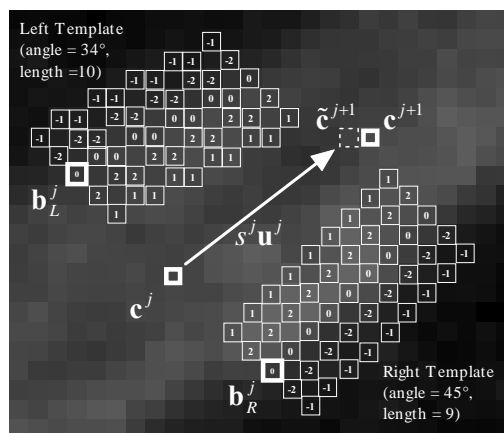


Fig. 10. Illustrates the iterative vessel/neurite tracing algorithm. Starting with initial seeds, the algorithm estimates the next location based on a robust estimate of the local boundary [2].

LIST OF TABLES

Table I. The eigenvalues of the Hessian matrix indicate common geometrical models in biological cell and tissue-level imagery, as shown [27]. For dark objects on bright backgrounds, the signs are reversed. In 2-D, the first two eigenvalues λ_1 and λ_2 are used and plate-like structures cannot be resolved. All three eigenvalues are used in 3-D.

Table II. The components of the parameter vector $\xi \in \mathbb{Z}^8$, their respective ranges, default values, and constraints on their values for the tracing algorithm.

Table III. Summary of experimental results with 223 images from four sources. The first two columns list the image sources, and number of images. For all experiments, 1000 RRS iterations were used, and an 8-dimensional parameter space was searched. The third column shows the improvements in the segmentation quality metric q when optimal parameter settings are computed for each image. The fourth column shows the improvements when settings are optimized for just one randomly selected image, and then applied to the rest of the images in the batch.

LIST OF FIGURES

Fig. 1. Optimal tracing settings lead to more accurate measurements. (a) A phase contrast image of cultured neurites grown on an imprinted surface with known orientations of 45° and 90° . (b) Automatically-generated traces using default settings. (c) Traces obtained with automatically selected parameters using the method presented in this paper. (d) The normalized angular histogram of measured segment orientations extracted from the automatically-generated traces. Note the correct peak at 45° obtained using automatically-selected settings vs. 34° using default settings. (Data courtesy: Dr. Gary Banker, OHSU).

Fig. 2. Illustrates the proposed self-optimizing image segmentation approach. Panel (a) shows a traditional segmentation algorithm in which the parameter settings ξ are set empirically for each input image \mathcal{I} . Panel (b) illustrates the proposed method in which a global optimization algorithm efficiently

explores the parameter space Ω driven by a segmentation quality assessment value based on trading off conciseness of the segmentation vs. its coverage. The user optionally specifies a single universal parameter to override the tradeoff.

Fig. 3. Venn diagrams illustrating the re-align and shrink operations in the exploitation step of the recursive random search algorithm (RRS). The current sample is denoted ξ_1 , and the local exploitation subspace is depicted as a un-shaded circle around it. After drawing a certain number of random samples within the current space \mathcal{S}_1 , if a better sample ξ_2 is found, then the search is re-aligned to the sample space \mathcal{S}_2 . If no better sample is found during the random sampling, the parameter space \mathcal{S}_1 is shrunk to \mathcal{S}_3 instead of realigning to \mathcal{S}_2 .

Fig. 4. Displays empirical and best-fit probability distribution function (PDF) of the vesselness values at the background regions \mathcal{B} in Panel (a) and at the foreground regions \mathcal{F} in Panel (b). Ranked by the Kolmogorov-Smirnov (KS) test statistic, the exponential distribution for \mathcal{B} (KS value 0.27) and the generalized-beta distribution for \mathcal{F} (KS value 0.05) were determined to be the best fit out of 15 distributions considered. The parameters of the best-fitted distributions were obtained using maximum-likelihood estimation.

Fig. 5. Trivial automatic thresholding example illustrating the behavior of the segmentation quality metric q . (a) Image of a fluorescently labeled neurite captured by a widefield microscope. (b) The multi-scale vesselness measure. (c) Plot of the metric q against the threshold τ value. (c) The optimal segmentation $\hat{\mathcal{M}}$ using $\hat{\tau} = 41$.

Fig. 6. An example varying just two parameters, $g \in [10, 30]$ and $\tau_c \in [1, 10]$, with others fixed at default values (Table II). Panel (a) shows a multi-photon microscope image of fluorescently-labeled neurites. Panel (b) displays the vesselness measure. Panel (c) shows the non-trivial optimization landscape. (d) Using the default parameter values ($g = 15, \tau_c = 3$). (e) The worst under-segmentation ($g = 26, \tau_c = 10$). (f) The worst over-segmentation ($g = 10, \tau_c = 1$). (g) The optimal segmentation ($g = 21, \tau_c = 8$).

Fig. 7. Illustrating applications of the proposed method to: (a) a human retinal fundus image; (b)-(d) images of cultured neurons. Default traces are shown in panels (e) through (h). Traces using automatically-selected settings using 1000 RRS trials are shown in panels (i) through (l). The quality improvement is 4% for the retina image in panel (a), 6% for the neuron image in panel (b), 7% for the neuron image in panel (c), and 38% for the neuron image on the micro-fabricated surface in panel (d).

Fig. 8. Displays the segmentation quality improvements on the batch of images from the Synaptic Distribution Study [69] as summarized in Table III. The fourth image from this batch is shown in Fig. 7b. The shaded bars show the percentage improvements in the segmentation quality metric when optimal parameter settings are computed for each image. The blank bars show the percentage improvements when settings are optimized for just one randomly selected image, and then applied to the rest of the images in the batch.

Fig. 9. Average percentage improvement in segmentation quality for all 223 test images (Table III). This plot illustrates the high efficiency of RRS during its early exploration of the global parameter space. The improvement between 500 and 1000 RRS trials is only 0.22%.

Fig. 10. Illustrates the iterative vessel/neurite tracing algorithm. Starting with initial seeds, the algorithm estimates the next location based on a robust estimate of the local boundary [2].